submitted to **Journal of Space Weather and Space Climate**

Ionospheric Plasma Structuring in Relation to Auroral Particle Precipitation

F. Enengl[1], D. Kotova[1], Y. Jin[1], L. B.N. Clausen[1], and W. J. Miloch[1]

Department of Physics, University of Oslo, Problemveien 7, 0315 Oslo
e-mail: florine.enengl@fys.uio.no

ABSTRACT

Auroral particle precipitation potentially plays a main role in ionospheric plasma structuring. The impact of auroral particle precipitation on plasma structuring is investigated using multi-point measurements from scintillation receivers and all sky cameras from Longyearbyen, Ny-Ålesund and Hornsund on Svalbard. This provides us with the unique possibility of studying the spatial and temporal dynamics of the aurora. Here we consider three case studies to investigate how plasma structuring is related to different auroral forms. We demonstrate that plasma structuring impacting the GNSS signals is largest at the edges of auroral forms. Here we studied two stable arcs, two dynamic auroral bands and a spiral. Specifically for arcs we find elevated phase scintillation indices at the pole-ward edge of the aurora. This is observed for auroral oxygen emissions (557.7 nm) at 150 km in the ionospheric E-region. This altitude is also used as the ionospheric piercing point for the GNSS signals as the observations remain the same regardless of different satellite elevations and azimuths. Further, there may be a time delay between the temporal evolution of aurora (f.e. commencement and fading of auroral activity) and observations of elevated phase scintillation indices. The time delay could be explained by the intense influx of particles, which increases the plasma density and causes recombination to carry on longer, which may lead to a persistence of structures - a 'memory effect'. High values of phase scintillation indices can be observed even shortly after strong visible aurora and can then remain significant at low intensities of the aurora.

Key words. particle precipitation, phase scintillation index, plasma structuring, ionospheric E-region

1. Introduction

The aurora can be seen as the signature of direct coupling of the ionosphere and magnetosphere. During high geomagnetic activity, energetic particle precipitation leads to higher intensity of the aurora resulting in different auroral forms. Dynamical processes in the E- and F- regions of the ionosphere are often associated with instabilities and turbulence which result in plasma structuring and irregularities at various scales. Such irregularities in ionospheric plasma density have impact on the propagation of radio waves (e.g., Keskinen and Ossakow, 1983; Huba et al.,

1985; Kintner and Seyler, 1985; Moen et al., 2013; Deshpande et al., 2014). Trans-ionospheric radio waves propagating through regions of density irregularities undergo diffraction and refraction, and they result in rapid fluctuations in phase and amplitude of the received signal, referred to as scintillation (e.g., Hey et al., 1946; Kintner et al., 2007). Scintillation of the received signal affects man-made systems, such as the radio communication and/or satellite based positioning systems. At the same time, scintillation of the received signal can be used as an indication for ionospheric plasma structuring. This will be also the approach in this work, where we will focus on the role of the auroral particle precipitation during geomagnetic substorms and investigate how different discrete auroral forms, i.e., stable arcs and fast moving forms (such as spirals), relate spatially and temporally to structuring in the ionospheric plasma density.

The Earth's ionosphere and magnetosphere are directly coupled in the polar regions via the Birkeland currents, which can be seen as drivers for the aurora. There is a variety of resulting auroral forms, which have been categorized over many years with regards to their shapes, process and lifetime, but to this day there is no clear and well accepted definition for all of the forms. Some auroral forms and their evolution can be linked to certain substorm phases (e.g., Akasofu, 1966; Elphinstone et al., 1996; Partamies et al., 2015). The auroral arcs are well-studied phenomena in quiet (for a review see Karlsson et al. (2020)) and active geomagnetic periods. Davis (1978) studied auroral arcs and their distortions into complex forms (spirals and curls) and defined an auroral arc as an recognizable luminosity resulting from the impingement of a field-aligned sheet beam of charged particles upon the atmosphere. The most simple form is an east-west elongated quiet discrete auroral arc. The width of the arc can be very thin (0.5-1.5 km) (Partamies et al., 2010), but most mesoscale size arcs have an observed width of around 10 km - 50 km (Knudsen et al., 2001). Arcs often appear in multiple- arc structures, and are found both during quiet and active periods. Multiple arc structures are arrays of arcs which are near-parallel to each other and in close proximity, and they are also the most common form of discrete auroral observations (Davis, 1978; Gillies et al., 2014). The multiple arc structures are referred to as arc packets when they are formed by splitting of the trailing arc into two, possibly due to the Alvén wave dispersion (Semeter et al., 2009). Stable and quiet auroral arcs are expected in the evening and at night-time. Here, we will study auroral emissions in the night time sector from 21h to 03h MLT (magnetic local time).
Other noteable auroral distortions are curl, spiral, bands, ray forms, westward travelling surge or omega bands (e.g., Elphinstone et al., 1996; Hallinan and Davis, 1970; Ivchenko et al., 2005; Partamies et al., 2017). In this paper we will focus on spiral structures. Spirals are larger scale auroral vertices (20-1300km), which form as the aurora twists counter-clock wise. It is suggested that the Kelvin-Helmholtz instability could play a role in formation of the spiral (Davis and Hallinan, 1976; Hallinan and Davis, 1970; Hallinan, 1976; Partamies et al., 2001). While Davis and Hallinan (1976); Keiling et al. (2009) relate spirals to magnetically disturbed periods, Partamies et al. (2001) relate them primarily to magnetically quiet conditions. However, fast-moving spirals, which signatures are only found in a single all-sky camera (ASC) image, seem to be related to an increasing geomagnetic activity (Partamies et al., 2001).
A variety of highly dynamic phenomena (e.g., polar cap patches, field aligned currents, high density F-region plasma, or particle precipitation) cause plasma irregularities in the E and F- region ionosphere (e.g., Moen et al., 2013; van der Meeren et al., 2015; Spogli et al., 2016; Jin et al., 2016, 2017; Fæhn Follestad et al., 2020). Ionospheric plasma structuring can be indirectly observed by

scintillation receivers. Recorded signals allow for calculating the phase and amplitude scintillation indices. At high latitudes, effect on irregularities on the trans-ionospheric wave can also be reflected in the degradation of the receiver tracking performance, Total Electron Content (TEC) jumps and cycle slips (Skone et al., 2001; Alfonsi et al., 2008; Moen et al., 2013; Chernyshov et al., 2020, & references therein).

Auroral particle precipitation can lead to significant plasma irregularities (Kelley et al., 1982; Keskinen and Ossakow, 1983; Weber et al., 1985; Prikryl et al., 2011), but it is still an open question to what extent it contributes to plasma structuring and whether it is dominant in the E or F-region ionosphere. It is observed that soft particle precipitation is unlikely the main source of the large-scale F-region plasma structures on the nightside (Jin et al., 2016). While on the dayside the main ionization source of the E-region is the EUV solar radiation, on the nightside Joule heating and auroral particles with energies of 10-30 keV dominate the energy input into the system (Millward et al., 1999; Wilson et al., 2006; Nikolaeva et al., 2021).

There have been previous studies that tried to answer this question. Kinrade et al. (2013) studied ionospheric irregularities caused by the auroral particle precipitation using scintillation receivers and auroral imagers located at the South Pole. They found spatially and temporally well-correlated scintillations with atomic oxygen emissions at wavelengths of λ=557.7 nm and 630.0 nm. This correlation is better for emissions at λ =557.7 nm, which could be due to the tracking method's effectiveness at two emission wavelengths of different characteristic intensities. They found optical images of aurorae to be a useful spatial and temporal indicator of the GPS phase scintillations during intense and persistent auroral activity, especially for discrete arcs and at the auroral boundary. Another study, by van der Meeren et al. (2015), sheds light on the Global Navigation Satellite System's (GNSS's) signal scintillations during intense substorm aurora. The data is recorded at GNSS receivers around Svalbard. They observed severe phase scintillation, which are following the intense pole-ward edge of the auroral oval as it expands pole-ward and show that received signals may experience strong scintillation when they intersect oxygen (λ=557.7 nm) emissions. The satellite systems of GPS, GLONASS and Galileo were affected similarly through the scintillations in relation to the intense line of sight auroral emissions in a highly localized region of the sky. Discrete aurora and GPS signal corruption have been studied by Semeter et al. (2017), using a network of receivers and imagers in Alaska. The ASC sampled images of oxygen emissions at λ = 558 nm. The auroral form of interest was a westward travelling surge and the loss of lock events consistently appeared at the edges of auroral forms. The scintillation regions were confined to a narrow strip (<20 km) tangential to the trailing edge of the observed aurora. As the appearance of the loss of lock events consistently followed the auroral boundaries irrespective of the satellite elevation and azimuth, the authors suggested the source to be near the oxygen 558 nm emission line. This is within the E-region of the ionosphere.

The questions i) in which layer of the ionosphere auroral particle precipitation plays a dominant role in plasma structuring and ii) what the spatial and temporal characteristics of the elevated scintillation indices with respect to different auroral forms are still remain open (e.g., Kinrade et al., 2013; van der Meeren et al., 2015; Jin et al., 2016; Semeter et al., 2017). In this paper, we will study how stable auroral arcs and fast moving forms (bands and spirals) relate spatially and temporally to ionospheric plasma structuring. The observations are made by using several scintillation receivers and ASCs located in Longyearbyen, Ny-Ålesund, and Hornsund on Svalbard. Case studies which

consider different auroral forms during the substorm events are presented. We observe elevated values of the phase scintillation index pole-ward of the arcs, and on the boundaries of fast moving forms. These characteristics have been found for the 557.7 nm oxygen emissions, indicating that the auroral particle precipitation in the E-region can contribute to relevant plasma structuring. We also observe a short time-delay between the onset of the aurora and observed plasma structuring.

2. Instruments and Approach

To study whether plasma structuring is driven by particle precipitation, we investigate the relative location between elevated scintillation indices and the aurorae. For this purpose we use data from three ASC on Svalbard. Two of the cameras are Keo Sentry 4ix Monochromatic Imagers from KEO Scientific, with filters, operated by the University of Oslo (UiO). They are situated in Longyearbyen (LYR, geographic coordinates: 78.15° N, 16.04° E) and in Ny-Ålesund (NYA, geographic coordinates 78.92° N, 11.93° E). The imagers record emission intensities every 30 s, with a field of view (FOV) of 180°. Both imagers are equipped with the narrow band filters to monitor 557.7 nm (green) and 630.0 nm (red) auroral emissions. For the analysis, the ASC images are projected to 150 km and 250 km (green and red auroral emission altitudes) respectively. The imager in Hornsund (HOR, geographic coordinates 77° N, 15.55° E) is a Sony A7 SII color camera with a FOV of 180 °, also operated by UiO. The availability of recorded images for this camera on the days of interest is every 15 minutes. The ASCs are used to determine the form of the aurora and its relative location to the observed elevated scintillation indices of Global Navigation Satellite Systems (GNSS) signals.

To analyse the impact of auroral particle precipitation on the GNSS signals, five GNSS ionospheric scintillation receivers on Svalbard are used in this study. The delay Δt of a signal propagating through a plasma is dependent on the electron density n_e and the signal frequency f:

$$\Delta t = \frac{40.3}{c f^2} \int n_e \, d\rho, \tag{1}$$

with c being the speed of light, ρ the ray path (e.g., Kintner et al., 2005, 2007).

The phase ϕ is connected to time delay Δt and therefore to electron density variations along the signal path (equation 1) through

$$\phi = f \Delta t \tag{2}$$

(e.g., Yeh and Liu, 1982; Kintner et al., 2007). As the phase is affected by the time delay and electron content variations it indicates plasma structuring processes. Phase scintillations are caused by large scale irregularities in a range of meters (above the Fresnel radius) to a few kilometers (e.g., Basu et al., 1998; Kintner et al., 2007). The phase scintillation index σ_ϕ,

$$\sigma_\phi = \langle \phi^2 \rangle - \langle \phi \rangle^2, \tag{3}$$

can be understood as the standard deviation of a measured phase and is dominated by large-scale fluctuations (Yeh and Liu, 1982; Kintner et al., 2007). Even though the index is not issue-free, e.g. due to the dominance of the low-frequency component of the phase power spectrum, the phase or related electron density variations nevertheless can indicate physical structuring in the ionosphere (Beach, 2006). Refractive and diffractive variations of σ_ϕ are not differentiated in this study, as we

use σ_ϕ as a measure of plasma structuring and to study the relative location to auroral forms, but are not studying the effects on the carrier phase. Amplitude scintillations are described by the amplitude scintillation index S_4

$$S_4 = \sqrt{\frac{\langle I^2 \rangle - \langle I \rangle^2}{\langle I \rangle^2}}. \tag{4}$$

(e.g., Briggs and Parkin, 1963; Yeh and Liu, 1982). The S_4 index describes and is effected by irregularities in a range of hundreds of meters to meters (at and below the Fresnel radius) (e.g., Basu et al., 1998; Kintner et al., 2007).

In this study, we use the calibrated 60-seconds reduced data (Oksavik, 2020a) of the phase (σ_ϕ) and amplitude (S_4) scintillation index. A cut-off angle of 15° is used on the scintillation data to minimize the multipath effects.

The data is recorded by NovAtel GPStation-6 receivers. The receiver in Hornsund is situated about 500 meters from the ASC and is run by the University of Oslo. The receivers situated in Ny-Ålesund (co-located with the NYA ASC), Longyearbyen (co-located with the LYR ASC), Bjørnøya (BJN, geographic coordinates 74.50° N, 19° E) and Hopen (HOP, geographic coordinates 76.51° N, 25.01° E) are operated by the University of Bergen (Oksavik, 2020b). The receivers track GPS, Galileo and GLONASS satellites. We use all received signals from these satellite systems as they have previously been shown to be similarly affected by ionospheric irregularities (van der Meeren et al., 2015).

The Interplanetary Magnetic Field (IMF) data and the solar wind conditions are downloaded from NASA/GSFC's OMNI data set through OMNIWeb (King and Papitashvili, 2005). We assess the IMF Bz magnetic field component, the solar wind flow speed and sym-H (1-min resolution GSM (geocentric solar magnetospheric coordinates) data). A negative IMF Bz component can indicate dayside reconnection. The sym-H index is a measure of the magnetospheric ring current intensity and used to quantify geomagnetic storms. The index is calculated using data from different magnetometer stations near the equator and describes the symmetric portion of the magnetic field horizontal component (Wanliss and Showalter, 2006). These indices help to describe and filter for background conditions and evaluate whether the geomagnetic conditions indicate geomagnetic storms. To investigate substorm conditions the horizontal component of the local magnetic field was used. It is recorded by a magnetometer network around Svalbard operated by the Tromsø Geophysical Observatory (Tanskanen, 2009). The decrease in the B_x component of the magnetic field at high latitudes is a signature of the enhancement of the westward electrojet and the substorm current wedge in superposition with eastward electrojet enhancements (Akasofu, 1965; D'Onofrio et al., 2014). Further we use the Kp index (from GFZ Potsdam and the National Geophysical Data Center), which is a proxy for the energy input from the solar wind to the magnetosphere. The Kp index is calculated based on 13 selected subauroral ground-based magnetic observatories and is the mean value of the disturbance levels in the horizontal magnetic field components. Higher Kp values correspond to stronger disturbances (Matzka et al., 2021).

3. Case Selection and Conditions

Data from the ASC network were used to select events for the case study. The first season (2019/2020) when all three cameras (NYA, LYR, HOR) were in operation and recorded data, is

considered for this study. The season is spanning from October-March. On 73 days all three ASCs have recorded data in an overlapping timespan (two hours). Days with a KP index lower than 2.5 were excluded. This reduced the set to 24 days. The solar wind conditions for each of the selected events are shown in Figure 1. Most of these days are part of six longer lasting multi-day (5+days) moderate geomagnetic storm events with high solar wind speeds (above 400 km/s; see panels b,e,h), negative sym-H component (-20 nT to -40 nT; see panels c,f,i), re-occuring negative Bz (see panels a,d,g) and negative drops of the local B_x component (shown in Figure 2 panels a,e,i). For comparability of the cases events with available data between 18-24 UT (21h-03h MLT nightside) were selected, this means the data set has been reduced to find times at which all three ASC recorded continuous data in the majority of the 18h-24h UT section. The set is now down-filtered to 12 days as remaining candidates for the case study. After the filtering process, the imagery was visually assessed and out of the days with intense auroral emissions the days with the least cloud cover (for all three ASC) that were part of different geomagnetic storm events were selected. The selected dates are the 28th October 2019, 29th January 2020 and the 22nd February 2020. The similarity in the events lies in the background conditions as all selected dates are substorm events with KP indices higher than 2.5. The events are in the night sector to meet similar geomagnetic conditions and types of the aurora. Particle precipitation is strongly visible on all of them. The randomness in the case study events is achieved through limited data availability and cloud cover on the ASC images, providing us a representative set of case studies with similar conditions, but spread over the whole season.

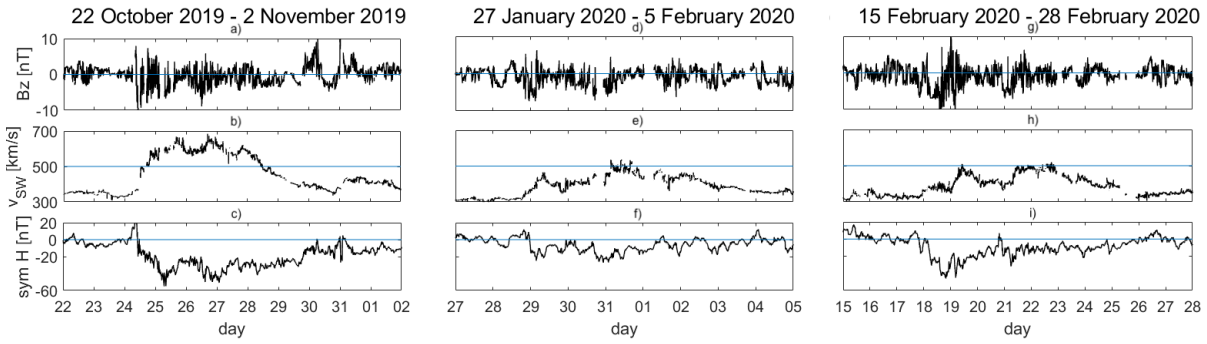

Fig. 1. Solar wind data recorded during the selected case study dates: 28th October 2019 (panels a-c), 29th January 2020 (d-f) and 22nd February 2020 (g-i). Panels a,d,g show the solar wind/ interplanetary magnetic field Bz component, indicating reconnection with Earth's magnetic field when negative. Panels b,e,h shows the solar wind flow speed which increases to over 400 km/s during geomagnetic storms, while the sym-H component (a measure of the ring current), shown in panels c,f,i, is abruptly negative during storms with a change of sym H > 20 nT.

4. Observations

Figure 2 shows data from the selected case study dates: 28th October 2019, 29th January 2020 and 22nd February 2020 from 18-24 UT. In panels (a,e,i) the horizontal magnetic field component B_x is shown. The decreases in B_x indicate substorm events at the respective stations (NYA-red,

LYR-green, HOP-black, BJN-orange, HOR-blue). Times of intense particle precipitation can be investigated by presenting the center pixel column of the ASC images as a time series- this time versus latitude plot is named a keogram. The keograms reveal times of auroral activity above zenith of the recording ASC. The keograms presented in panels (b,f,j) show images that originate from the LYR ASC using the filter for 557.7 nm (green) emissions. Here we associate the auroral activity, visible bright auroral emissions, with times of particle precipitation. Panels (c,g,k) and (d,h,l) show σ_ϕ and $S4$ scintillation index data recorded by the scintillation receivers in the respective stations. The indices are used to quantify plasma structuring in location, intensity and scale. $S4$ indicates plasma structuring on scales down a few meters, below the Fresnel radius, while σ_ϕ indicates structuring above the Fresnel radius (hundreds of meters to km).

4.1. Altitude of Plasma Structuring

Different regions in the ionosphere are influenced by different phenomena characteristic for the specific altitudes ranges. Determining the altitude in which the GNSS signals are disrupted is crucial to relate the disturbances observed through the phase scintillation index to physical phenomena. The images of green and red auroral emissions are projected to their estimated emission altitudes (150 km and 250 km respectively). The scintillation indices are projected to different altitudes (piercing points) to find out whether the observed disturbances happen in the same altitude range as the auroral emissions and whether they correspond better to the green or red emissions. For this, different piercing points between 100 km to 350 km were tested. For the green auroral emissions (150 km), it is observed that for lower (100 km) or higher (200 km) piercing point altitudes, the elevated σ_ϕ values appear randomly placed with regards to the auroral forms. When observing small patches of auroral emissions further east/west of zenith, one observes the elevated σ_ϕ values further east/west of the patch when the ionospheric piercing point is chosen low/high. However, when choosing the same altitude as piercing point as the green auroral emission altitude, we find that the elevated σ_ϕ values at the boundaries and aligning well with the evolution of auroral forms. Using imagery from all three ASC and all five receivers, elevated σ_ϕ values are consistently found at the edges of the auroral forms for this piercing point altitude. This behaviour is observed for chosen piercing point for satellites regardless of satellite azimuth or elevation, just as in Semeter et al. (2017). The elevated σ_ϕ values are increased at the boundaries of the auroral emissions, invariant with different satellite elevations. Another evidence for this is given when projecting data of only the co-located imager and scintillation receiver on the same plot, a case where the mapping altitude is irrelevant. We again observe elevated σ_ϕ values at the pole-ward edges of the aurora, see the video using data from only the NYA ASC and NYA scintillation receiver in supplementary material. This indicates that the signal is impacted right at the altitude of green auroral emission. This behavior has not been detected in the same extent with regards to red auroral emissions.

The emission altitude of green auroral emissions is used as the piercing point altitude for the study along with ASC images of the green auroral emissions.

4.2. Case Studies: Spatial and Temporal Evolution of Plasma Structuring

ASC imagery of the three case study events is shown in this section. The ASC images (green aurora projected to 150 km) are plotted onto the geographical coordinates and a map of Svalbard shown in contrast. On top of that the observed phase scintillation data (piercing point 150 km) is displayed.

The phase scintillation data is referred to as slightly elevated σ_ϕ above 0.2 rad, moderately elevated σ_ϕ above 0.3 rad, strongly elevated σ_ϕ above 0.5 rad and very strongly elevated σ_ϕ above 0.7 rad. Not all of the measured data during auroral activity of that day is shown: very faint aurora, forms that are not classified as part of a process showing arcs/spirals/bands, forms that are mostly cut off by the FOV or repetitive images are excluded. The auroral activity is fluctuating in intensity, and can decrease to low intensity values or vanish shortly from the observation location before it onsets again. Whether low intensity aurora and no aurora is observed is difficult to distinguish, as it depends on the chosen intensity scale what will be visible. In the following, intensities measured under 10 kR-NYA/20 kR-LYR are referred as no visible aurora. This threshold has been chosen as the elevated phase scintillation index is not observed in combination with intensities under 10 kR for NYA and 20 kR for LYR before the auroral onset. It can however be observed after the aurora vanished, this may have other reasons than auroral emissions below 10 kR/20 kR as discussed later. Only the representative images are shown in the results, but the remaining images were combined to videos attached in supplementary material. In the following especially the high intensity values of the aurora may be influenced by the way the camera and brightness is calibrated and calculated. They are however a good measure for comparison between and relation to the σ_ϕ indices.

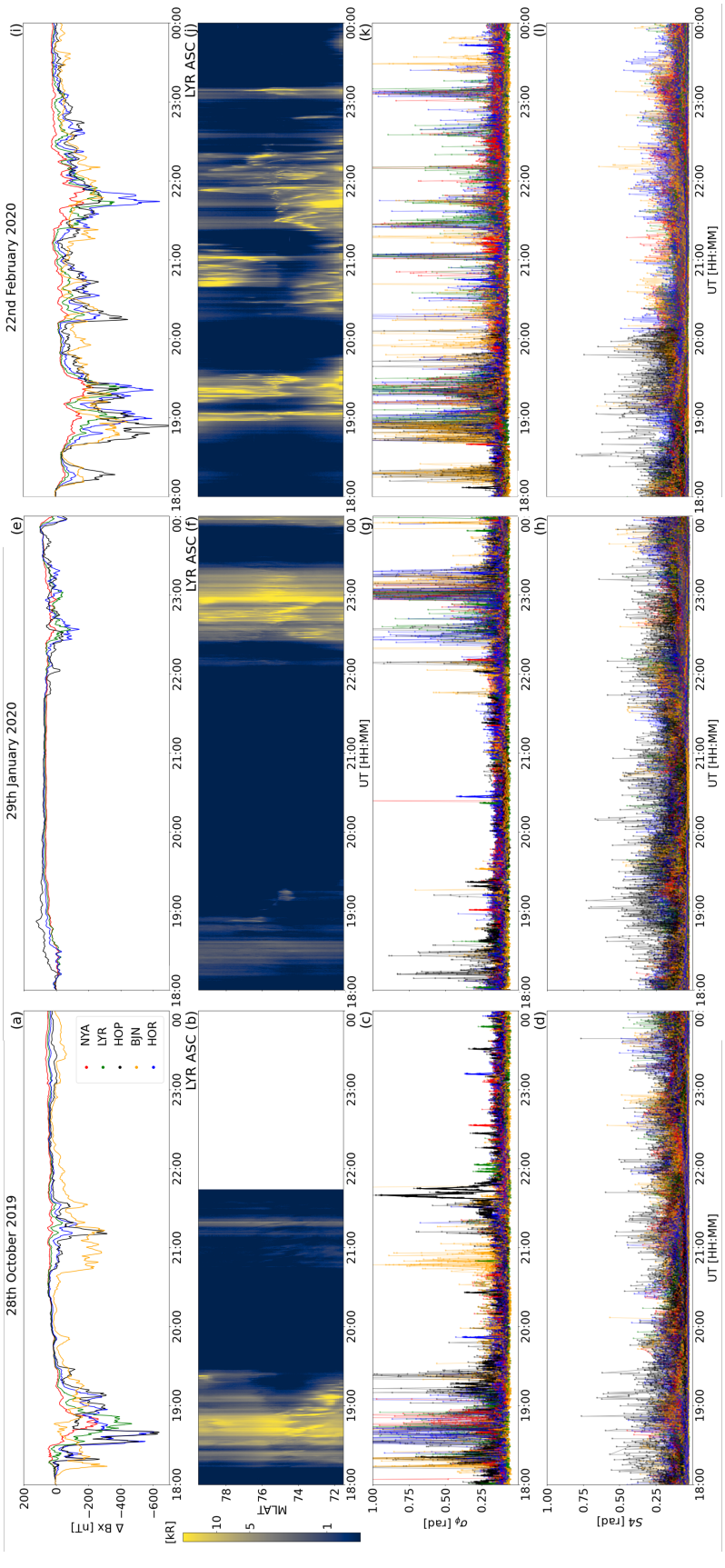

Fig. 2. Data from the selected events: 28th October 2019, 29th January 2020 and 22nd February 2020 from 18-24 UT. In panels (a,e,i) the horizontal magnetic field component B_x is shown. The dips indicate substorm events at the respective stations (NYA-red, LYR-green, HOP-black, BJN-orange, HOR-blue). Panels (b,f,j) shows the 557.7 nm emissions intensity observed by the LYR ASC in form of a keogram. The bright auroral emissions correspond to times of particle precipitation. Panels (c,g,k) and (d,h,l) show σ_ϕ and S4 scintillation index data recorded by the scintillation receivers in the respective stations. They quantify the location, scale and intensity of plasma structuring.

4.2.1. 28th October 2019

The first selected event of this season is the 28th October 2019, see Figure 2(a-d). The local magnetic field B_x component shows a decrease between 18:10-19:30 UT measured at NYA (shown in red), LYR (green), HOP (black), BJN (orange), HOR (blue) and indicating a substorm. At HOP the magnitude of the decrease is especially large, up to a change of -600 nT in the B_x component, followed by HOR and LYR. A less severe decrease in the B_x component is observed around 20:40-21:40 UT (strongest in BJN and HOP, lightest in LYR and NYA). At the same time auroral activity is observed with the LYR ASC. Intense precipitation lasts from 18:15 to 19:30 UT and light precipitation from 20:45-21:20 UT. The latter shows only faint aurora, which is also reflected in the B_x component measurements, where we observed only light variations for LYR. Elevated σ_ϕ coincides with particle precipitation between from 18:15 to 19:30 UT, this is observed for all stations. The later time interval or particle precipitation is likewise accompanied by elevated σ_ϕ, but disturbances are not in all stations recorded. BJN (panel c, shown in orange) records elevated σ_ϕ about 25 minutes before the strongest emissions are observed at LYR (panel b), but σ_ϕ increases right as the B_x component at BJN drops. The response of S4 to the particle precipitation is not as clear as for σ_ϕ, but a slight increase of S4 especially in the measurements at HOP (panel a, shown in black) may be observed around 19 UT. Elevated S4 values can be an indication for diffractive effects (Yeh and Liu, 1982), but are not discussed here.

The 28th October 2019 observations indicate a substorm event, auroral emissions and disturbances in the phase scintillation index between around 18:10-19:30 UT and 20:40-21:40 UT (Figure 2). This long and intense auroral activity can be best viewed from the NYA ASC as shown in Figure 3. The Figure shows a time evolution (a) to (h) from when the auroral activity commences to when it fades out. This arc is also observed from the HOR ASC and LYR ASC. Videos of the arc from the NYA and LYR station are shown in the supplementary material. In Figure 3a at 18:29:23 UT light auroral activity (<30 kR) starts in the south-east quarter of the ASC's FOV, no elevation of σ_ϕ is observed at this stage. A minute later, at 18:30:23 UT, the auroral activity is at double its intensity (>60 kR) forming a faint arc. No elevation of σ_ϕ values is yet measured. At 18:31:23 UT the auroral intensity is reaching its intensity maximum (>80kR) and now very strongly elevated σ_ϕ values are observed in the east. The delay between auroral emissions until elevated σ_ϕ values are observed is in this case 2 minutes. The underlying processes causing elevated σ_ϕ values/ plasma structuring may come with a time delay related to the recombination rates of the precipitating electrons arriving in the E-region ionosphere. The fast flows of the injected electrons could drive a two-stream instability. The difference in drift velocity between the electrons and ions, which collide with neutrals, could in specific drive the modified two-stream instability, the Farley-Buneman instability (Farley Jr., 1963). Shortly after, at 18:31:38 UT, very strongly elevated σ_ϕ values measured poleward of the established auroral arc (with an intensity still over >80 kR) are oberved. Instabilities working specifically at the boundary of the particle stream may be dominant at this point, leading to very localized elevated σ_ϕ values along the pole-ward boundary. Note that the plasma density is lower at the pole-ward boundary than the equator-ward boundary. The intensity fluctuates (down to <60 kR), but the σ_ϕ values stay elevated over the next 9 minutes. At 18:40:23 UT a second arc (with an intensity <40 kR) forms in the center of the ASC image combined with very strongly elevated σ_ϕ. The southern arc is still very intense (>80 kR) with pole-ward very strongly elevated σ_ϕ values. At 18:45:23 UT the arc in the center intensifies (>60 kR) and moderately elevated σ_ϕ values are

observed pole-ward of the central arc and stronger elevated σ_ϕ values between the arcs. The southern arc has faded out (with an intensity < 45 kR). At 15:52:38 UT the arc structure is dissolved and the intensity is decreased to similar values (<60 kR) as at 18:30:23 UT (before we observed elevated σ_ϕ). Occasional very strong σ_ϕ values are still observed alongside strong and moderate σ_ϕ values. This could be due to a 'memory effect', the precipitation has moved away, but the E-region ionosphere has not yet restored its original state and electrons may still recombine and structures persist until the amount of excess particles has declined. At 18:54:23 UT, the intensity (<30 kR) has decreased to its starting values (panel a). However occasional moderately to strongly elevated σ_ϕ values are measured. Eastwards, a low intensity auroral patch is co-located with a very strongly elevated σ_ϕ value. The E-region ionosphere is still unstable as the structuring process continues even for weak auroral emissions.

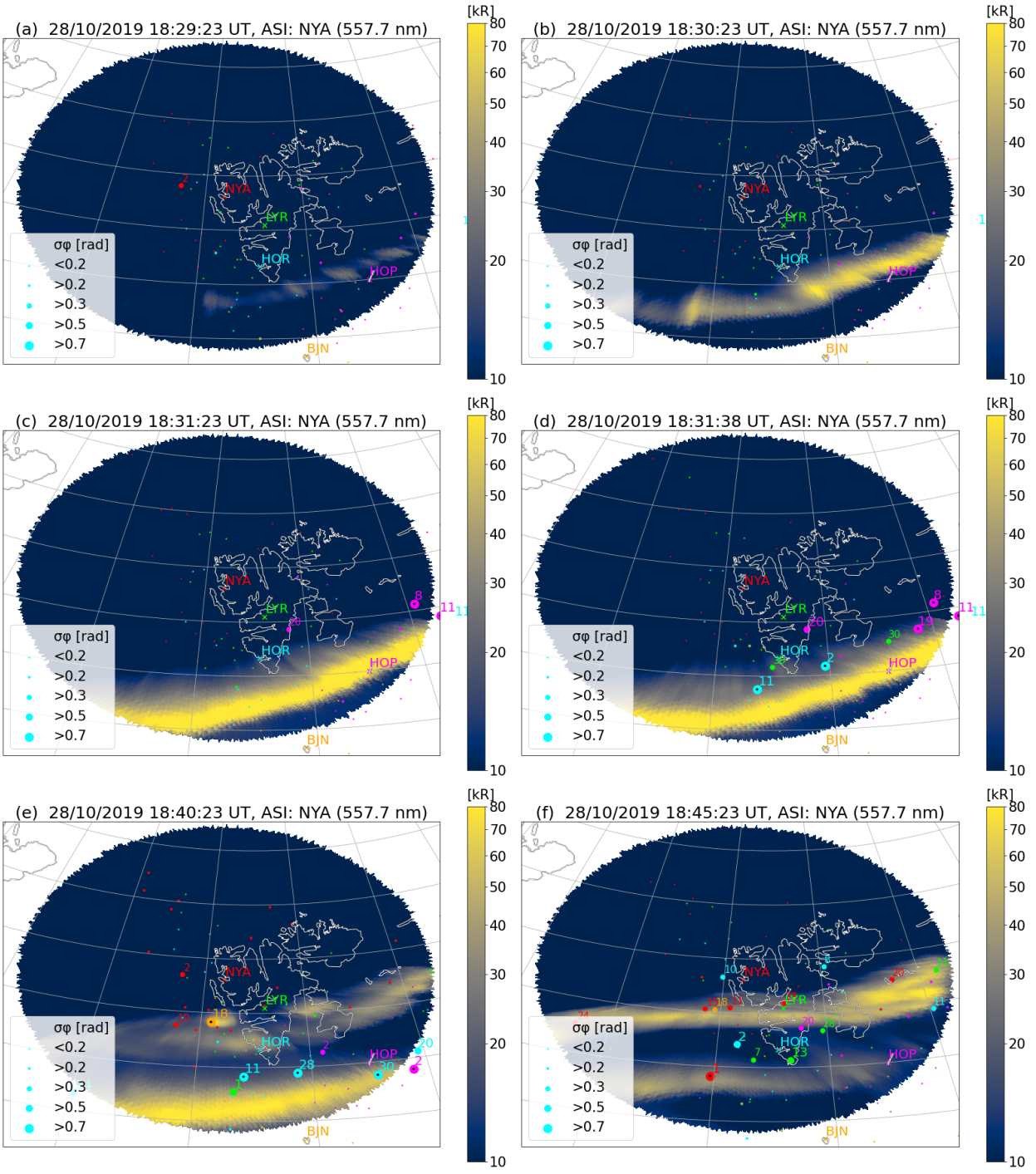
(a) 28/10/2019 18:29:23 UT, ASI: NYA (557.7 nm)
(b) 28/10/2019 18:30:23 UT, ASI: NYA (557.7 nm)
(c) 28/10/2019 18:31:23 UT, ASI: NYA (557.7 nm)
(d) 28/10/2019 18:31:38 UT, ASI: NYA (557.7 nm)
(e) 28/10/2019 18:40:23 UT, ASI: NYA (557.7 nm)
(f) 28/10/2019 18:45:23 UT, ASI: NYA (557.7 nm)
σφ [rad]
<0.2
>0.2
>0.3
>0.5
>0.7
NYA
LYR
HOR
HOP
BJN
[kR]
80
70
60
50
40
30
20
10

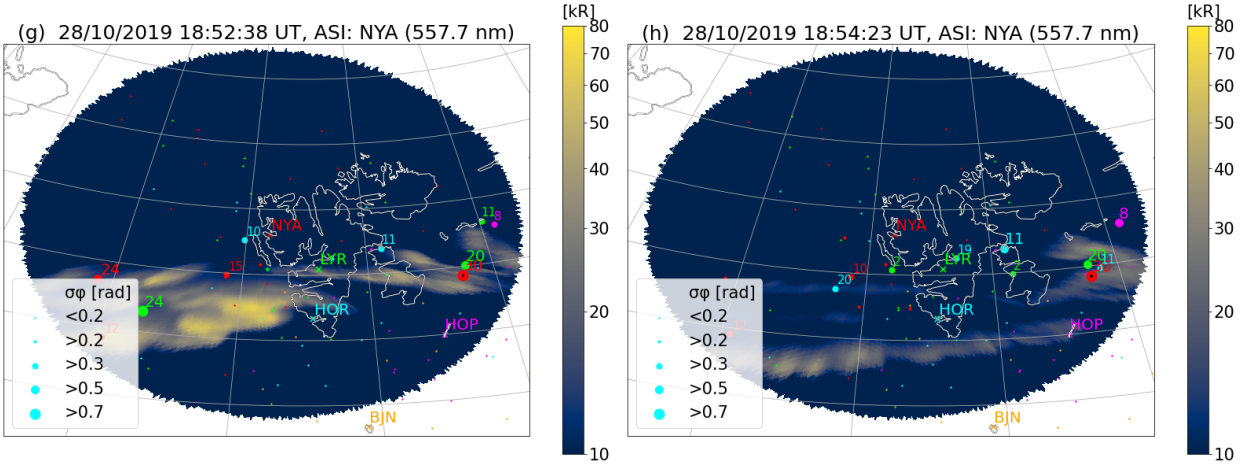

Fig. 3. The projection of the 557.7 nm emissions shown together with the phase scintillation index σ_ϕ over a map of Svalbard and geographical longitude/latitude on 28th October 2019 as seen from the NYA ASC for different time instances. Brighter yellow auroral emissions mean stronger intensity and bigger markers mean stronger σ_ϕ. The markers represent σ_ϕ measurements from NYA in red, LYR in green, HOR in cyan, HOP in magenta and BJN in orange. Panels a and b show the commencement of an auroral arc. Panels c and d show the arc at its maximum intensity (>80kR). In panel d we can point out the very strongly elevated σ_ϕ pole-ward of the arc. Panels e and f show two auroral arcs and corresponding σ_ϕ values. Panels g and h show fading of the aurora and decrease in σ_ϕ. Even though panels a and h show similar auroral intensities (<30kR) they show different levels of σ_ϕ: panel a - no elevated σ_ϕ, panel h - different levels of elevated σ_ϕ. The aurora shown in this figure is classified as arcs.

4.3. 29th January 2020

On the 29th January 2020 decreases in the local B_x component and strong auroral particle precipitation combined with increases in σ_ϕ values are observed, see Figure 2(e-h). There are minor variations in the B_x component (about 50 nT) and light precipitation between 18 and 19 UT (panel f). After 21:50 UT a fluctuations in the local B_x components is observed. The dip in B_x reaches its local minimum at a change of around -200 nT at 22:20, a change much weaker than in the first studied case. Nevertheless, the auroral emissions are intense, especially around 23 UT. The σ_ϕ values are elevated strongly in the same time frame as precipitation is observed. The S4 index does not show an as strong correlation to particle precipitation as σ_ϕ. In Figure 4 the event is shown as observed by the LYR ASC. The first 30 minutes the auroral activity is fluctuating and moderately elevated σ_ϕ values are found for faint aurora (<45 kR). One example is shown at 22:53:08 UT where moderately elevated σ_ϕ values are measured, but the auroral emissions are beneath (<30 kR). Whether there is a time delay in this selected case between the auroral onset and the elevated σ_ϕ values or not is difficult to determine as the auroral activity does not increase monotonically here as in the case on 28th October 2019. At 22:55:53 UT the intensity increases (>80 kR) and moderately to strongly elevated σ_ϕ values located within and surrounding the auroral form are measured. A high intensity spiral-shaped aurora (>80 kR) is observed at 22:56:38 UT with very strongly elevated σ_ϕ. A spiral-shaped aurora has previously been linked to the Kelvin-Helmholtz instability (Hallinan, 1976). The strongly elevated σ_ϕ values follow the boundary of the auroral spiral neatly, just as in 3d where the elevated σ_ϕ values follow the pole-ward boundary of the auroral arc. At 22:57:38 UT, the auroral spiral and high intensity area has grown. We continue to observe very strongly elevated σ_ϕ values at the boundary of the form, but now also within the form. At the boundaries of the spiral form, we observe primarily elevated σ_ϕ values pole-ward of the form and only rarely equator-ward. A minute later at 22:58:38 UT the form has shrank and is still surrounded by very strongly elevated σ_ϕ values. Elevated σ_ϕ values continue to be observed for over 15 minutes after the auroral intensity decreased below 40 kR. At 23:14:23 UT the auroral intensity is beneath 30 kR and very strongly elevated σ_ϕ values are still observed. This is another indication that there may be longer lasting structuring processes, after the precipitation has declined. The observations are confirmed by the NYA and HOR cameras. The images recorded by the LYR and NYA camera for this event are attached as videos in the supplementary material.

4.4. 22nd February 2020

On the 22nd of February multiple local negative changes in B_x, auroral emissions and elevated σ_ϕ values are measured, see Figure 2(i-l). In this event also S4 is elevated, mostly in the section before 20:30 UT (panel l). The forms before 20:30 UT are very turbulent and fast moving (video of data from all three imagers shown in the supplementary material). The data before 20:30 UT are due to its fast and dynamic forms not conclusive on the spatial relation between auroral forms and elevated σ_ϕ values. Here we discuss the auroral forms after 20:30 UT as viewed from the LYR ASC. In Figure 5, at 21:00:38 UT, a band has formed in the east. The band appears fast and intense (>60kR), with immediate strongly to very strongly elevated σ_ϕ values on the north-westward boundary of the band. No time delay between the abrupt and intense auroral onset and elevated σ_ϕ values is observed. At 21:02:08 UT the intensity has reached over 80 kR and the elevated σ_ϕ values are found in the center of the band. Here, the elevated σ_ϕ values are first observed at the

boundary, but the form expands and intensifies so that the elevated σ_ϕ values move into the band-shape. Note that more GNSS satellites are crossing the band / are close to the band equator-ward of HOR, but none of these are experiencing elevated σ_ϕ values. Barely any satellites are in the band's vicinity above NYA latitudes. At 21:02:28 UT the auroral band starts fading out (<70 kR) leaving very strongly elevated σ_ϕ values pole-ward of the band. This is another example of how elevated σ_ϕ values are still measured for faint auroral activity. A single-point very strongly elevated σ_ϕ index can still be observed until three minutes after intense aurora. Only an auroral patch (<50 kR) is still visible in the east, here shown at 21:04:53 UT. After some minutes without strong activity, a faint auroral band (<50 kR) moves into the FOV around 21:21:53 UT. At 21:23:23 the form has increased its intensity to over 80 kR but only a slightly elevated σ_ϕ value is observed. Over one minute later at 21:24:38 UT the high intensity area of the aurora grows bigger and very strongly elevated σ_ϕ values are found at the boundaries, especially pole-ward. Here we see again, how the auroral activity grows and expands before elevated σ_ϕ values are observed. At 21:25:52 UT the form becomes more complex, still reaching over 80 kR, and strongly to very strongly elevated σ_ϕ values are measured at the boundaries and within the form. At 21:32:38 UT (7 minutes later) the auroral intensity has decreased (<50 kR) and only moderately to slightly elevated σ_ϕ values are observed pole-ward of the band shaped aurora. In both here presented cases, elevated σ_ϕ values are measured for faint aurora, suggesting plasma structuring to continue after the auroral activity has declined. On the 22nd February 2020 we observe fast-moving forms, and the elevated σ_ϕ values are not solely found pole-ward but also equator-ward. As they are changing more rapidly than the other forms, the elevated σ_ϕ values may be following the auroral activity with a delay.

5. Discussion

We have studied elevated phase scintillation indices in relation to regions of auroral emission with data from three different substorm events in detail. Three distinct auroral forms were considered: arcs, spirals and bands. While the observed arcs were stable, the other forms were more dynamic. The first selected substorm event (28th October 2019) shows arcs. For the first observed arc, we found a delay in the onset of elevated σ_ϕ values of 2 minutes, from when auroral activity (<30 kR) was observed, see again Figure 3a-c. The very strongly elevated σ_ϕ values are then observed at the pole-ward edge of the arc (Figure 3d-f) and between multiple arcs (3e,f). Even for faint aurora, very strongly elevated σ_ϕ values are measured for at least 2 minutes after the auroral intensity has decreased to under 60 kR, Figure 3g-h, moderately elevated σ_ϕ values are observed for over 4 minutes after. In the substorm event on 29th January 2020 an auroral spiral was observed. For the spiral, the intensity is not monotonically increasing as it was for the arc. Moderately elevated σ_ϕ values are observed even for faint Aurora (<30 kR), see again Figure 4a. The elevated σ_ϕ values are observed on the edges of the auroral spiral, see Figure 4c-e. Over 10 minutes after the auroral intensity decreases under 60 kR very strongly elevated σ_ϕ values are still measured, see Figure 4f. The last of the studied substorm events (22nd February 2020) shows auroral bands. The abrupt and fluctuating intensity during the onset of the band caused auroral emissions with elevated σ_ϕ to be observed right away without a delay, see Figure 5a. The second band first shows emissions above 60 kR and it takes over a minute to observe elevated σ_ϕ values, see Figure 5e. For both bands we observe elevated σ_ϕ values at the pole-ward boundary of the auroral form, see Figure 5(b,d&f,g). For the first band elevated σ_ϕ values are observed also at the west-ward boundary and within the

form, see Figure 5b. When the auroral bands fade out, elevated σ_ϕ values are still observed over 1 to 7 minutes (first and second example respectively), see Figure 5(c,d & g,h).

In summary, we observed: (1) Elevated phase scintillation indices correspond consistently well to the spatial and temporal evolution of auroral forms in the green emissions (oxygen, 557.7 nm) altitudes, which means particle precipitation into the ionospheric E-region is a driver for plasma structuring. (2) There may be a time delay between the temporal evolution of aurora (f.e. commencement and fading of auroral activity) and elevated phase scintillation index measurements. (3) The elevated phase scintillation indices are observed at the boundary of the auroral emissions (poleward for discrete and stable arcs and on all boundaries for bands and spirals).

When the ionospheric piercing point for the navigation satellites is chosen at the same altitude as the projections of the green (557.7 nm) auroral emissions, the elevated σ_ϕ values are consistently observed on the auroral edges, invariant of their elevation and azimuth. The same behaviour is found when using only the co-located ASC and scintillation receiver (see the video with data from the NYA ASC and scintillation receiver in supplementary material), a case where the mapping altitude becomes irrelevant. Thus we suggest the σ_ϕ values to be effected at the altitude of the green auroral emissions. This means that E-region irregularities and instabilities cause observed plasma structuring. The findings are in agreement with Kinrade et al. (2013); Semeter et al. (2017), who also find better correlation of observed elevated phase scintillation indices with the 557.7 nm auroral emissions.

Previous studies, from e.g. van der Meeren et al. (2014); Jin et al. (2016), linked phase scintillation mainly to the polar cap F-region ionosphere (especially to polar cap patches and tongues of ionization). The effects of intense local particle precipitation in the auroral oval on elevated σ_ϕ has been studied and referred to as a blobs type II by Jin et al. (2016). They also state that soft F-region particle precipitation does not contribute much to plasma structuring processes in the nightside auroral region. Our findings are in agreement with this, but we however show that more energetic particle precipitation penetrating down to the E-region may be a main source and is found co-located with intense elevated σ_ϕ. The link between elevated σ_ϕ or phase scintillations and E-region auroral particle precipitation has also been observed by several authors (e.g., Kinrade et al., 2013; Forte et al., 2017; Loucks et al., 2017; Sreenivash et al., 2020; Makarevich et al., 2021).

The time delay strongly depends on the auroral dynamics with regards to auroral intensity. For a case where the aurora appears out of quiet conditions and the auroral intensity increases monotonically, the phase scintillation indices are elevated around 1 (2) minutes after the intensity reached over 60 kR (30 kR), see again the example of the auroral arc or the second auroral band. This is at a level on which simultaneous and co-located aurora and phase scintillation index enhancements are commonly found, even without further increases to higher intensity levels. The duration time delay depends strongly on which intensity is used as a threshold. When the auroral intensity is increasing (decreasing) non-monotonically, it the time delay may be even longer (shorter). In case of the spiral, or, the first auroral band considered, the elevated σ_ϕ is observed right after a prompt increase in auroral intensity.

As the auroral intensity decreases monotonically, elevated σ_ϕ is observed down to levels of under 20 kR. Especially when the auroral intensity is fluctuating around these levels, we observe occasionally high elevated scintillation indices. We have observed elevated σ_ϕ between 1 to over 7 minutes after auroral intensities dropped back under 60 kR. The effect of a time-delay after decreasing auroral emissions is stronger than the time-delay of the elevated σ_ϕ value onset. Both may only be

reached for certain conditions. For stable forms, the relation may be more clear than for dynamic forms.

Particle precipitation is a signature observed as a part of field-aligned currents (Carter et al., 2016; Xiong et al., 2020). They couple the magnetosphere to the ionosphere and can cause severe phase scintillations through direct driving of the ionospheric plasma by structured precipitation or electric fields resulting in elevated scintillation indices (Boström, 1964; Fæhn Follestad et al., 2020). Particle precipitation is usually observed in times of high convection and convection patterns were investigated with SuperDARN. We see a two cell pattern (during southward Bz) for the studied dates. We do not observe strong flows on the nightside, and experience mostly growth in the cells, linking to dayside reconnection (Dungey, 1961; Juusola et al., 2014). The negative By component is prominent for the 29 January 2020, peaking at 22:00 UT the time we observe the spiral form, and is driving an asymmetric ionospheric convection pattern (e.g., Weimer, 1995). During times of particle precipitation, the twin cell convection pattern covers Svalbard and with this precipitation area.

We propose that the time delay may occur through a 'memory effect'. Particle precipitation into the ionospheric E-region enhances conductance and causes a widespread irregularity dissipation and redistribution of energy (e.g., Ivarsen et al., 2021). The influx of particles increases the plasma density leading to ionization and prolonging recombination. When the particle precipitation declines or moves, it will still take some time for plasma structures to diffuse. The structuring process initiated during particle precipitation will carry on. Instabilities in the plasma lead to further structuring processes, irregularity dissipation and redistribution of energy.

The location of the elevated phase scintillation indices is also dependent on the spatial and temporal auroral dynamics. When investigating a stable discrete auroral form, such as the arc, we observe strongly elevated σ_ϕ (> 0.5 rad) solely at the pole-ward boundary. If the form is faster moving, such as for spirals or bands, elevated σ_ϕ may be seen even westward or equator-ward, but nevertheless on the boundaries. Fast-moving forms may move away quicker from the measurement location while elevated σ_ϕ value are still observed at this location. For spirals and bands, elevated σ_ϕ are observed also on the east and westward boundaries as well as on the boundaries within the shape. Semeter et al. (2017) studied loss of lock (LL) events and their correlation with discrete auroral emissions. They studied mostly fast-moving auroral forms, and found LL events on equator-ward (trailing) edge of the auroral form, while the form is moving pole-ward. This agrees with our results, as we propose that there is a time delay in the elevated scintillation index measurements. Therefore, for fast-moving pole-ward forms, the LL events would be observed equator-ward as the form moved past the measurement location further pole-ward. They note that although the pole-ward side of the arc has a similar or even greater density gradient, no LL events were observed there. This explanation may be valid in our case, as we propose that the structuring process in fact happens pole-ward, but the a fast-moving form has simply moved from its original place as the structuring persists. This however would not explain the cases where we observe pole-ward elevated σ_ϕ values at multiple stable arcs, as the equator-ward edge of the most pole-ward arc has a higher density gradient than the pole-ward boundary of an equator-ward arc. Unless the equator-ward arcs are sufficiently more intense than the pole-ward arcs, then the density gradient would be higher on the pole-ward edge of equator-ward arcs (see Figure 3e and f with two arcs).

The energy source for driving instabilities in the E-region ionosphere can be manifold, such from as flow shears, from gradients or directly by kinetic energy. Instabilities associated with particle

precipitation are e.g. kinetic instabilities, two-stream instabilities. The flow of particles in field-aligned currents can also produce current-driven instabilities (e.g., Kropotkin, 2016).

One instability that can be directly produced by a velocity shear (by particle precipitation/ electron beam) along the direction of or perpendicular to an externally imposed magnetic field is the Kelvin-Helmholtz instability (D'Angelo and Goeler, 1966; Hallinan and Davis, 1970; Pécseli, 2013). It can drive curls, or spirals as observed in the aurora (Hallinan and Davis, 1970).

Another relevant instability that may explain the observed plasma structuring is the Farley-Buneman instability (Farley Jr., 1963; Buneman, 1963; Treumann, 1997). The instability arises from the difference of the electron and ion velocity, caused by collisions of the ions with neutrals (Farley Jr., 1963). These conditions are given in the equatorial and polar E-region ionosphere, where this instability is typically found (Rogister and D'Angelo, 1970; Pécseli, 2013).

Various instabilities can arise in the ionosphere driven by e.g. currents, energetic particle streams or density gradients. However, the Kelvin-Helmholtz and Farley-Buneman instability do not only satisfy the encountered background conditions (E-region ionosphere, particle stream, collisions, availability of neutrals), but could also explain the observed behaviour of elevated σ_ϕ observations at the edges of different auroral forms (spirals, arcs, bands), the boundaries between the injected particles and the ionospheric E-region plasma.

The Kelvin-Helmholtz instability is extracting energy out of a shear flow along a boundary (Treumann, 1997) and is associated with auroral spirals (Hallinan and Davis, 1970). This may explain why we measure elevated σ_ϕ values on the outer boundaries and on boundaries whithin auroral spirals. The Farley-Buneman instability provides a more general explanation for plasma structuring observed at boundaries of different auroral forms, not only spirals. The auroral form boundaries are where the electrons stream past ions, which collide with neutrals, which is what feeds the Farley-Buneman instability (Farley Jr., 1963; Buneman, 1963). While the Kelvin-Helmholtz instability is working on bigger scales, the Farley-Buneman instability is operating on smaller scales. Multiple instabilities may be responsible for the plasma structuring processes we observe. Whether it is the difference in plasma density gradient that drives plasma structuring predominately at pole-ward edges of auroral arcs remains remains unknown. Further case studies with even higher spatial and temporal resolution are needed to understand the structuring process and to confirm which instability can cause delayed structuring processes in the E-region at the boundaries of auroral forms and at pole-ward boundaries for auroral arcs.

6. Conclusion

In this study, the relation between auroral particle precipitation and plasma structuring was investigated. In summary, the temporal and spatial evolution of auroral forms and phase scintillation indices were studied. For this, three event days with similar background conditions (substorm events, particle precipitation and nightside events) showing clear strong auroral emissions were selected. Data was available from three ASI imagers (NYA, LYR and HOR) and five scintillation receivers (NYA, LYR and HOR, HOP, BJN). This provides us with 18 h of data in which we observed auroral forms such as arcs, spirals and bands. Our results show that:

– (1) Elevated phase scintillation indices correspond consistently (invariant of satellite elevation and azimuth) to the spatial and temporal evolution of auroral forms when an ionospheric piercing

point for navigation satellites is chosen the same as the estimated green emissions (557.7 nm) altitude (150 km). This suggests that plasma structuring in the ionospheric E-region is an important driver for phase scintillations.

- (2) There may be a time delay between the temporal evolution of aurora (e.g. commencement and fading of auroral activity) and elevated phase scintillation index measurements. Particle precipitation enhances the plasma density. When the precipitation declines or moves, it will still take some time for the plasma structures to diffuse. Until then, instabilities will further cause redistribution of energy and irregularity dissipation.

- (3) The elevated phase scintillation indices are observed at the boundary of the auroral emissions. For discrete and stable arcs elevated phase scintillation indices are predominately observed pole-ward and for faster moving shapes, including spirals and bands, on the boundaries of the form. The irregularities and instabilities causing the elevated phase scintillation indices especially in the E-region may be due to instabilities which are driven by energy at the boundary of auroral forms, such as the Kelvin-Helmholtz instability (directly produced by a velocity shear such as from particle precipitation) or Farley-Buneman instability (through fast flows at the boundaries). Plasma structuring may predominately be observed on pole-ward boundary as the gradient in plasma density is larger than it is on the equator-ward boundary.

The question on why plasma structuring processes in the E-region are observed specifically at the edges of auroral forms, such as spirals and bands, and at polew-ard boundaries for auroral arcs remains open. Further case studies with even higher spatial and temporal resolution and bigger statistical studies investigating time-delay statistics are needed to understand the structuring process. In the future we also need to investigate further, which instabilities are caused during the plasma structuring processes and how they effect trans-ionospheric radio waves.

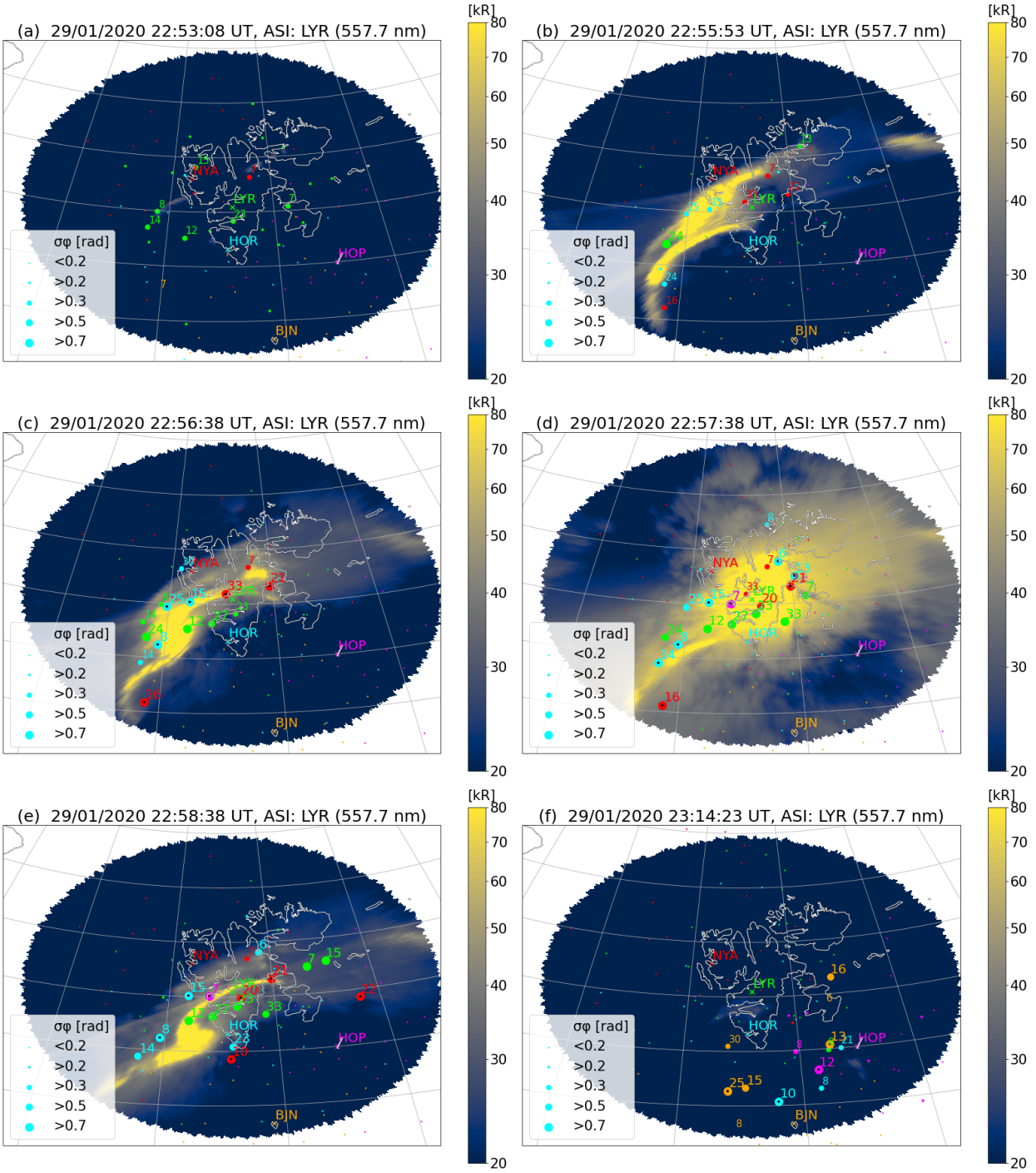

Fig. 4. The projection of the 557.7 nm emissions shown together with the phase scintillation index σ_ϕ over a map of Svalbard and geographical longitude/latitude on 29th January 2020 as seen from the LYR ASC for different time instances. Brighter yellow auroral emissions mean stronger intensity and bigger markers mean stronger σ_ϕ. The markers represent σ_ϕ measurements from NYA in red, LYR in green, HOR in cyan, HOP in magenta and BJN in orange. Panel a shows elevated σ_ϕ values yet without strong Aurora. Panel b shows strong auroral emissions and paired with elevated σ_ϕ values. In panels c, d and e an auroral spiral has formed and the elevated σ_ϕ values are primarily observed at the boundary of the auroral spiral. In panel f elevated σ_ϕ values on top of the faded out form. The aurora shown in this figure is classified as a spiral.

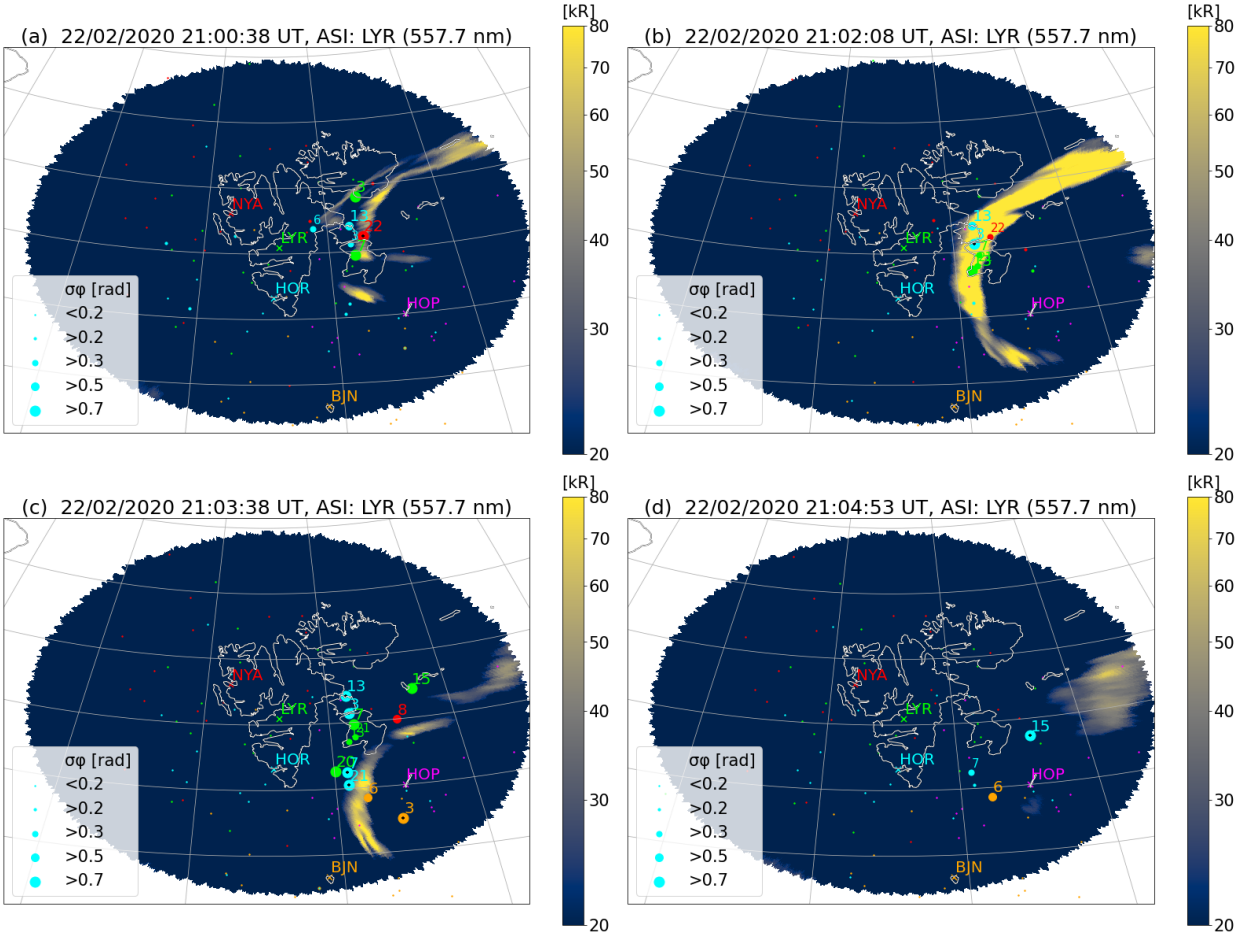
(a) 22/02/2020 21:00:38 UT, ASI: LYR (557.7 nm)
(b) 22/02/2020 21:02:08 UT, ASI: LYR (557.7 nm)
(c) 22/02/2020 21:03:38 UT, ASI: LYR (557.7 nm)
(d) 22/02/2020 21:04:53 UT, ASI: LYR (557.7 nm)
[kR]
80
70
60
50
40
30
20
σφ [rad]
<0.2
>0.2
>0.3
>0.5
>0.7
NYA
LYR
HOR
HOP
BJN

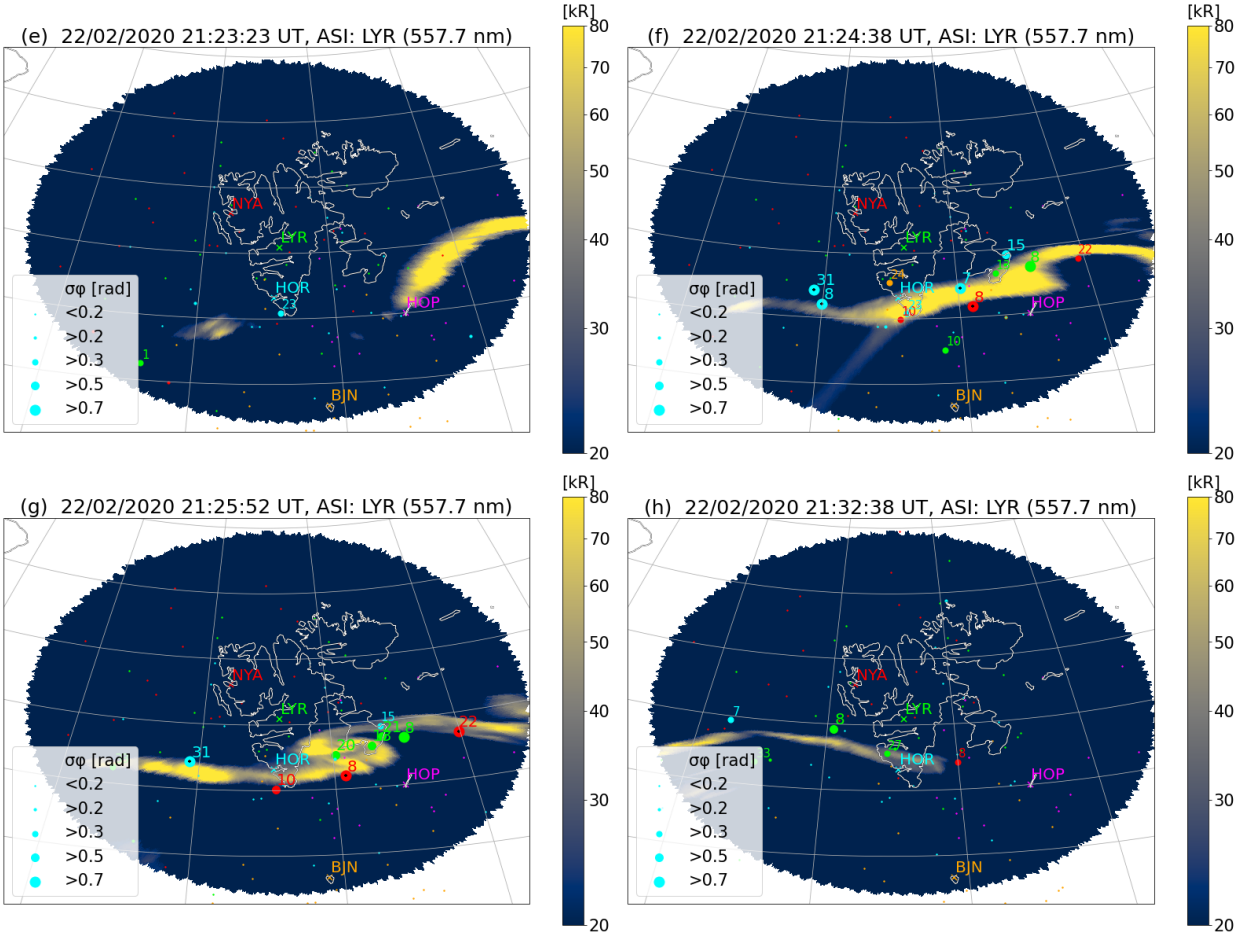

Fig. 5. The projection of the 557.7 nm emissions shown together with the phase scintillation index σ_ϕ over a map of Svalbard and geographical longitude/latitude on 22nd February 2020 as seen from the LYR ASC for different time instances. Brighter yellow auroral emissions mean stronger intensity and bigger markers mean stronger σ_ϕ. The markers represent σ_ϕ measurements from NYA in red, LYR in green, HOR in cyan, HOP in magenta and BJN in orange. Panel a shows a band-shaped Aurora and elevated σ_ϕ values west-ward. Panel b shows the intensified band, no with even stronger σ_ϕ values. Panels c and d show the fading of the auroral band, however σ_ϕ is still elevated. Panel e shows the commencement of the next auroral band, yet without strong elevated σ_ϕ values. Panels f and g show stronger auroral emissions paired with elevated σ_ϕ values at the boundary of the auroral band. In panel h elevated σ_ϕ is observed pole-ward of the fading auroral band. The aurora shown in this figure is classified as bands.

Acknowledgements. The authors thank Bjørn Lybekk for the maintenance of the all-sky imager and scintillation receiver data. The UiB Global Navigation Satellite System Data Collection was collected under Research Council of Norway contracts 212014 and 223252. Data from Hornsund have been acquired at the Polish Polar Station Hornsund in collaboration with the Institute of Geophysics, Polish Academy of Sciences. This study is in part supported by the European Research Council, European Research Council under the European Union's Horizon-2020 research and innovation programme (Grant Agreement No. 866357, POLAR-4DSpace). We thank the institutes who maintain the IMAGE Magnetometer Array: Tromsø Geophysical Observatory of UiT the Arctic University of Norway (Norway), Finnish Meteorological Institute (Finland), Institute of Geophysics Polish Academy of Sciences (Poland), GFZ German Research Centre for Geosciences (Germany), Geological Survey of Sweden (Sweden), Swedish Institute of Space Physics (Sweden), Sodankylä Geophysical Observatory of the University of Oulu (Finland), and Polar Geophysical Institute (Russia).

References

Akasofu, S.-I., 1965. Dynamic morphology of auroras. *Space science reviews.*, **4**(4), 498. 2

Akasofu, S.-I., 1966. The auroral oval, the auroral substorm, and their relations with the internal structure of the magnetosphere. *Planetary and Space Science*, **14**(7), 587–595. Https://doi.org/10.1016/0032-0633(66)90043-2, URL https://www.sciencedirect.com/science/article/pii/0032063366900432. 1

Alfonsi, L., A. J. Kavanagh, E. Amata, P. Cilliers, E. Correia, et al., 2008. Probing the high latitude ionosphere from ground-based observations: The state of current knowledge and capabilities during IPY (2007-2009). *JOURNAL OF ATMOSPHERIC AND SOLAR-TERRESTRIAL PHYSICS*, **70**(18, SI), 2293–2308. Greenland Space Science Symposium (GSSS-2007), Kangerlussuaq, GREENLAND, MAY 04-09, 2007, 10.1016/j.jastp.2008.06.013. 1

Basu, S., E. J. Weber, T. W. Bullett, M. J. Keskinen, E. MacKenzie, P. Doherty, R. Sheehan, H. Kuenzler, P. Ning, and J. Bongiolatti, 1998. Characteristics of plasma structuring in the cusp/cleft region at Svalbard. *Radio Science*, **33**(6), 1885–1899. Https://doi.org/10.1029/98RS01597, https://agupubs.onlinelibrary.wiley.com/doi/pdf/10.1029/98RS01597, URL https://agupubs.onlinelibrary.wiley.com/doi/abs/10.1029/98RS01597. 2, 2

Beach, T. L., 2006. Perils of the GPS phase scintillation index. *Radio Science*, **41**(5). Https://doi.org/10.1029/2005RS003356, URL https://agupubs.onlinelibrary.wiley.com/doi/abs/10.1029/2005RS003356. 2

Boström, R., 1964. A model of the auroral electrojets. *Journal of Geophysical Research*, **69**(23), 4983–4999. 5

Briggs, B., and I. Parkin, 1963. On the variation of radio star and satellite scintillations with zenith angle. *Journal of Atmospheric and Terrestrial Physics*, **25**(6), 339–366. Https://doi.org/10.1016/0021-9169(63)90150-8, URL https://www.sciencedirect.com/science/article/pii/0021916963901508. 2

Buneman, O., 1963. Excitation of field aligned sound waves by electron streams. *Physical review letters*, **10**(7), 285–287. 5

Carter, J. A., S. E. Milan, J. C. Coxon, M.-T. Walach, and B. J. Anderson, 2016. Average field-aligned current configuration parameterized by solar wind conditions. *Journal of Geophysical Research: Space Physics*, **121**(2), 1294–1307. Https://doi.org/10.1002/2015JA021567, https://agupubs.onlinelibrary.wiley.com/doi/pdf/10.1002/2015JA021567, URL https://agupubs.onlinelibrary.wiley.com/doi/abs/10.1002/2015JA021567. 5

Chernyshov, A. A., W. J. Miloch, Y. Jin, and V. I. Zakharov, 2020. Relationship between TEC jumps and auroral substorm in the high-latitude ionosphere. 1

D'Angelo, N., and S. v. Goeler, 1966. Investigation of the Kelvin-Helmholtz Instability in a Cesium Plasma. *The Physics of fluids (1958)*, **9**(2), 309–313. 5

Davis, T., 1978. Observed characteristics of auroral forms. *Space science reviews*, **22**(1), 77–113. 1

Davis, T. N., and T. J. Hallinan, 1976. Auroral spirals, 1. Observations. *Journal of Geophysical Research (1896-1977)*, **81**(22), 3953–3958. Https://doi.org/10.1029/JA081i022p03953, https://agupubs.onlinelibrary.wiley.com/doi/pdf/10.1029/JA081i022p03953, URL https://agupubs.onlinelibrary.wiley.com/doi/abs/10.1029/JA081i022p03953. 1

Deshpande, K. B., G. S. Bust, C. R. Clauer, C. L. Rino, and C. S. Carrano, 2014. Satellite-beacon Ionospheric-scintillation Global Model of the upper Atmosphere (SIGMA) I: High-latitude sensitivity study of the model parameters. *JOURNAL OF GEOPHYSICAL RESEARCH-SPACE PHYSICS*, **119**(5), 4026–4043. 10.1002/2013JA019699. 1

D'Onofrio, M., N. Partamies, and E. Tanskanen, 2014. Eastward electrojet enhancements during substorm activity. *Journal of Atmospheric and Solar-Terrestrial Physics*, **119**, 129–137. Https://doi.org/10.1016/j.jastp.2014.07.007, URL https://www.sciencedirect.com/science/article/pii/S1364682614001722. 2

Dungey, J. W., 1961. Interplanetary Magnetic Field and the Auroral Zones. *Physical review letters.*, **6**(2), 47–48. 5

Elphinstone, R. D., J. S. Murphree, and L. L. Cogger, 1996. What is a global auroral substorm? *Reviews of Geophysics*, **34**(2), 169–232. Https://doi.org/10.1029/96RG00483, https://agupubs.onlinelibrary.wiley.com/doi/pdf/10.1029/96RG00483, URL https://agupubs.onlinelibrary.wiley.com/doi/abs/10.1029/96RG00483. 1

Farley Jr., D. T., 1963. A plasma instability resulting in field-aligned irregularities in the ionosphere. *Journal of Geophysical Research (1896-1977)*, **68**(22), 6083–6097. Https://doi.org/10.1029/JZ068i022p06083, https://agupubs.onlinelibrary.wiley.com/doi/pdf/10.1029/JZ068i022p06083, URL https://agupubs.onlinelibrary.wiley.com/doi/abs/10.1029/JZ068i022p06083. 4.2.1, 5

Forte, B., C. Coleman, S. Skone, I. Häggström, C. Mitchell, F. Da Dalt, T. Panicciari, J. Kinrade, and G. Bust, 2017. Identification of scintillation signatures on GPS signals originating from plasma structures detected with EISCAT incoherent scatter radar along the same line of sight. *Journal of Geophysical Research: Space Physics*, **122**(1), 916–931. Https://doi.org/10.1002/2016JA023271, https://agupubs.onlinelibrary.wiley.com/doi/pdf/10.1002/2016JA023271, URL https://agupubs.onlinelibrary.wiley.com/doi/abs/10.1002/2016JA023271. 5

Fæhn Follestad, A., K. Herlingshaw, H. Ghadjari, D. J. Knudsen, K. A. McWilliams, J. I. Moen, A. Spicher, J. Wu, and K. Oksavik, 2020. Dayside Field-Aligned Current Impacts on Ionospheric Irregularities. *Geophysical Research Letters*, **47**(11), e2019GL086,722. E2019GL086722 10.1029/2019GL086722, https://doi.org/10.1029/2019GL086722, https://agupubs.onlinelibrary.wiley.com/doi/pdf/10.1029/2019GL086722, URL https://agupubs.onlinelibrary.wiley.com/doi/abs/10.1029/2019GL086722. 1, 5

Gillies, D. M., D. J. Knudsen, E. F. Donovan, E. L. Spanswick, C. Hansen, D. Keating, and S. Erion, 2014. A survey of quiet auroral arc orientation and the effects of the interplanetary magnetic field. *Journal of Geophysical Research: Space Physics*, **119**(4), 2550–2562. Https://doi.org/10.1002/2013JA019469, https://agupubs.onlinelibrary.wiley.com/doi/pdf/10.1002/2013JA019469, URL https://agupubs.onlinelibrary.wiley.com/doi/abs/10.1002/2013JA019469. 1

Hallinan, T. J., 1976. Auroral spirals, 2. Theory. *Journal of Geophysical Research*, **81**(22), 3959–3965. 1, 4.3

Hallinan, T. J., and T. Davis, 1970. Small-scale auroral arc distortions. *Planetary and space science*, **18**(12), 1735,in1,1737–1736,in4,1744. 1, 5

Hey, J. S., S. J. Parsons, and J. W. Phillips, 1946. Fluctuations in Cosmic Radiation at Radio-Frequencies. *Nature (London)*, **158**(4007), 234–234. 1

Huba, J. D., A. B. Hassam, I. B. Schwartz, and M. J. Keskinen, 1985. Ionospheric turbulence: Interchange instabilities and chaotic fluid behavior. *Geophysical research letters*, **12**(1), 65–68. 1

Ivarsen, M. F., J.-P. St-Maurice, Y. Jin, J. Park, W. Miloch, A. Spicher, Y.-S. Kwak, and L. B. N. Clausen, 2021. Steepening Plasma Density Spectra in the Ionosphere: The Crucial Role Played by a Strong E-Region. *Journal of Geophysical Research: Space Physics*, **126**(8), e2021JA029,401. E2021JA029401 2021JA029401, https://doi.org/10.1029/2021JA029401, https://agupubs.onlinelibrary.wiley.com/doi/pdf/10.1029/2021JA029401, URL https://agupubs.onlinelibrary.wiley.com/doi/abs/10.1029/2021JA029401. 5

Ivchenko, N., E. M. Blixt, and B. S. Lanchester, 2005. Multispectral observations of auroral rays and curls. *Geophysical Research Letters*, **32**(18). Https://doi.org/10.1029/2005GL022650, https://agupubs.onlinelibrary.wiley.com/doi/pdf/10.1029/2005GL022650, URL https://agupubs.onlinelibrary.wiley.com/doi/abs/10.1029/2005GL022650. 1

Jin, Y., J. I. Moen, W. J. Miloch, L. B. N. Clausen, and K. Oksavik, 2016. Statistical study of the GNSS phase scintillation associated with two types of auroral blobs. *Journal of geophysical research. Space physics*, **121**(5), 4679–4697. 1, 5

Jin, Y., J. I. Moen, K. Oksavik, A. Spicher, L. B. Clausen, and W. J. Miloch, 2017. GPS scintillations associated with cusp dynamics and polar cap patches. *Journal of space weather and space climate*, **7**, A23. 1

Juusola, L., S. E.Milan, M. Lester, A. Grocott, and S. M.Imber, 2014. Interplanetary magnetic field control of the ionospheric field-aligned current and convection distributions. *Journal of Geophysical Research: Space Physics*, **119**(4), 3130–3149. Https://doi.org/10.1002/2013JA019455, https://agupubs.onlinelibrary.wiley.com/doi/pdf/10.1002/2013JA019455, URL https://agupubs.onlinelibrary.wiley.com/doi/abs/10.1002/2013JA019455. 5

Karlsson, T., L. Andersson, D. Gillies, K. Lynch, O. Marghitu, N. Partamies, N. Sivadas, and J. Wu, 2020. Quiet, Discrete Auroral Arcs—Observations. *Space science reviews*, **216**(1). 1

Keiling, A., V. Angelopoulos, J. Weygand, O. Amm, E. Spanswick, et al., 2009. THEMIS ground-space observations during the development of auroral spirals. *Annales geophysicae*, **27**(11), 4317–4332. 1

Kelley, M. C., J. F. Vickrey, C. W. Carlson, and R. Torbert, 1982. On the origin and spatial extent of high-latitude F region irregularities. *Journal of Geophysical Research: Space Physics*, **87**(A6), 4469–4475. 1

Keskinen, M. J., and S. L. Ossakow, 1983. Theories of high-latitude ionospheric irregularities: A review. *Radio science*, **18**(6), 1077–1091. 1

King, J., and N. Papitashvili, 2005. Solar wind spatial scales in and comparisons of hourly Wind and ACE plasma and magnetic field data. *J. Geophys. Res.*, **A02104**, 110. 2

Kinrade, J., C. N. Mitchell, N. D. Smith, Y. Ebihara, A. T. Weatherwax, and G. S. Bust, 2013. GPS phase scintillation associated with optical auroral emissions: First statistical results from the geographic South Pole. *Journal of Geophysical Research: Space Physics*, **118**(5), 2490–2502. Https://doi.org/10.1002/jgra.50214, https://agupubs.onlinelibrary.wiley.com/doi/pdf/10.1002/jgra.50214, URL https://agupubs.onlinelibrary.wiley.com/doi/abs/10.1002/jgra.50214. 1, 5

Kintner, P., B. Ledvina, P. M. Kintner, and B. M. Ledvina, 2005. The ionosphere, radio navigation, and global navigation satellite systems. *Advances in space research : the official journal of the Committee on Space Research*, **35**(5), 788–811. 2

Kintner, P. M., B. M. Ledvina, and E. R. de Paula, 2007. GPS and ionospheric scintillations. *Space weather*, **5**(9), n/a. 1, 2, 2, 2, 2

Kintner, P. M., and C. E. Seyler, 1985. The status of observations and theory of high latitude ionospheric and magnetospheric plasma turbulence. *Space science reviews*, **41**(1-2), 91–129. 1

Knudsen, D. J., E. F. Donovan, L. L. Cogger, B. Jackel, and W. D. Shaw, 2001. Width and structure of mesoscale optical auroral arcs. *Geophysical Research Letters*, **28**(4), 705–708. Https://doi.org/10.1029/2000GL011969, https://agupubs.onlinelibrary.wiley.com/doi/pdf/10.1029/2000GL011969, URL https://agupubs.onlinelibrary.wiley.com/doi/abs/10.1029/2000GL011969. 1

Kropotkin, A., 2016. Formation of the small-scale structure of auroral electron precipitations. *Journal of Atmospheric and Solar-Terrestrial Physics*, **148**, 39–47. Https://doi.org/10.1016/j.jastp.2016.08.009, URL https://www.sciencedirect.com/science/article/pii/S1364682616302048. 5

Loucks, D., S. Palo, M. Pilinski, G. Crowley, I. Azeem, and D. Hampton, 2017. High-latitude GPS phase scintillation from E region electron density gradients during the 20–21 December 2015 geomagnetic storm. *Journal of Geophysical Research: Space Physics*, **122**(7), 7473–7490. Https://doi.org/10.1002/2016JA023839, https://agupubs.onlinelibrary.wiley.com/doi/pdf/10.1002/2016JA023839, URL https://agupubs.onlinelibrary.wiley.com/doi/abs/10.1002/2016JA023839. 5

Makarevich, R. A., G. Crowley, I. Azeem, C. Ngwira, and V. V. Forsythe, 2021. Auroral E-Region as a Source Region for Ionospheric Scintillation. *Journal of Geophysical Research: Space Physics*, **126**(5), e2021JA029,212. E2021JA029212 2021JA029212, https://doi.org/10.1029/2021JA029212, https://agupubs.onlinelibrary.wiley.com/doi/pdf/10.1029/2021JA029212, URL https://agupubs.onlinelibrary.wiley.com/doi/abs/10.1029/2021JA029212. 5

Matzka, J., C. Stolle, Y. Yamazaki, O. Bronkalla, and A. Morschhauser, 2021. The Geomagnetic Kp Index and Derived Indices of Geomagnetic Activity. *Space weather*, **19**(5), n/a. 2

Millward, G. H., R. J. Moffett, H. F. Balmforth, and A. S. Rodger, 1999. Modeling the ionospheric effects of ion and electron precipitation in the cusp. *Journal of Geophysical Research: Space Physics*, **104**(A11), 24,603–24,612. 1

Moen, J. I., K. Oksavik, L. Alfonsi, Y. R. Dåbakk, V. Romano, and L. Spogli, 2013. Space weather challenges of the polar cap ionosphere. 1

Nikolaeva, V., E. Gordeev, T. Sergienko, L. Makarova, and A. Kotikov, 2021. AIM-E: E-Region Auroral Ionosphere Model. *Atmosphere.*, **12**(6), 748. 1

Oksavik, K., 2020a. Documentation of GNSS Total Electron Content and Scintillation Data (60 s) at Svalbard. *DataverseNO*. Https://doi.org/10.18710/EA5BYX. 2

Oksavik, K., 2020b. The University of Bergen Global Navigation Satellite System Data Collection. *DataverseNO*. Https://doi.org/10.18710/AJ4S-X394. 2

Partamies, N., L. Juusola, D. Whiter, and K. Kauristie, 2015. Substorm evolution of auroral structures. *Journal of geophysical research. Space physics*, **120**(7), 5958–5972. 1

Partamies, N., K. Kauristie, T. I. Pulkkinen, and M. Brittnacher, 2001. Statistical study of auroral spirals. *Journal of Geophysical Research: Space Physics*, **106**(A8), 15,415–15,428. Https://doi.org/10.1029/2000JA900172, https://agupubs.onlinelibrary.wiley.com/doi/pdf/10.1029/2000JA900172, URL https://agupubs.onlinelibrary.wiley.com/doi/abs/10.1029/2000JA900172. 1

Partamies, N., M. Syrjäsuo, E. Donovan, M. Connors, D. Charrois, D. Knudsen, and Z. Kryzanowsky, 2010. Observations of the auroral width spectrum at kilometre-scale size. *Annales geophysicae*, **28**(3), 711–718. 1

Partamies, N., J. M. Weygand, and L. Juusola, 2017. Statistical study of auroral omega bands. *Annales geophysicae*, **35**(5), 1069–1083. 1

Prikryl, P., L. Spogli, P. T. Jayachandran, J. Kinrade, C. N. Mitchell, et al., 2011. Interhemispheric comparison of GPS phase scintillation at high latitudes during the magnetic-cloud-induced geomagnetic storm of 5-7 April 2010. *ANNALES GEOPHYSICAE*, **29**(12), 2287–2304. 10.5194/angeo-29-2287-2011. 1

Pécseli, H. L., 2013. Waves and oscillations in plasmas. 5

Rogister, A., and N. D'Angelo, 1970. Type II irregularities in the equatorial electrojet. *Journal of Geophysical Research*, **75**(19), 3879–3887. 5

758 Semeter, J., S. Mrak, M. Hirsch, J. Swoboda, H. Akbari, et al., 2017. GPS Signal Corruption by the
759 Discrete Aurora: Precise Measurements From the Mahali Experiment. *Geophysical Research Letters*,
760 **44**(19), 9539–9546. Https://doi.org/10.1002/2017GL073570, https://agupubs.onlinelibrary.
761 wiley.com/doi/pdf/10.1002/2017GL073570, URL https://agupubs.onlinelibrary.wiley.
762 com/doi/abs/10.1002/2017GL073570. 1, 4.1, 5

763 Semeter, J., M. Zettergren, M. Diaz, and S. Mende, 2009. Wave dispersion and the discrete aurora: New con-
764 straints derived from high-speed imagery (vol 113, art no A12208, 2008). *JOURNAL OF GEOPHYSICAL*
765 *RESEARCH-SPACE PHYSICS*, **114**. 1

766 Skone, S., K. Knudsen, and M. de Jong, 2001. Limitations in GPS receiver tracking performance under
767 ionospheric scintillation conditions. *Physics and chemistry of the earth. Part A, Solid earth and geodesy*,
768 **26**(6-8), 613–621. 1

769 Spogli, L., C. Cesaroni, D. Di Mauro, M. Pezzopane, L. Alfonsi, et al., 2016. Formation of ionospheric
770 irregularities over Southeast Asia during the 2015 St. Patrick's Day storm. *JOURNAL OF GEOPHYSICAL*
771 *RESEARCH-SPACE PHYSICS*, **121**(12), 12,211–12,233. 10.1002/2016JA023222. 1

772 Sreenivash, V., Y. Su, and S. Datta-Barua, 2020. Automated Ionospheric Scattering Layer
773 Hypothesis Generation for Detected and Classified Auroral Global Positioning System
774 Scintillation Events. *Radio Science*, **55**(1), e2018RS006,779. E2018RS006779 2018RS006779,
775 https://doi.org/10.1029/2018RS006779, https://agupubs.onlinelibrary.wiley.com/doi/pdf/
776 10.1029/2018RS006779, URL https://agupubs.onlinelibrary.wiley.com/doi/abs/10.
777 1029/2018RS006779. 5

778 Tanskanen, E., 2009. A comprehensive high-throughput analysis of substorms observed by
779 IMAGE magnetometer network: Years 1993-2003 examined. *J. Geophys. Res.*, **114, A05204**.
780 Https://doi.org/10.1029/2008JA013682. 2

781 Treumann, R. A., 1997. Advanced space plasma physics. 5

782 van der Meeren, C., K. Oksavik, D. Lorentzen, J. I. Moen, and V. Romano, 2014. GPS scintillation
783 and irregularities at the front of an ionization tongue in the nightside polar ionosphere. *Journal of*
784 *Geophysical Research: Space Physics*, **119**(10), 8624–8636. Https://doi.org/10.1002/2014JA020114,
785 https://agupubs.onlinelibrary.wiley.com/doi/pdf/10.1002/2014JA020114, URL https:
786 //agupubs.onlinelibrary.wiley.com/doi/abs/10.1002/2014JA020114. 5

787 van der Meeren, C., K. Oksavik, D. A. Lorentzen, M. T. Rietveld, and L. B. N. Clausen, 2015. Severe and
788 localized GNSS scintillation at the poleward edge of the nightside auroral oval during intense substorm
789 aurora. 1, 2

790 Wanliss, J. A., and K. M. Showalter, 2006. High-resolution global storm index: Dst versus SYM-H.
791 *Journal of Geophysical Research: Space Physics*, **111**(A2). Https://doi.org/10.1029/2005JA011034,
792 https://agupubs.onlinelibrary.wiley.com/doi/pdf/10.1029/2005JA011034, URL https:
793 //agupubs.onlinelibrary.wiley.com/doi/abs/10.1029/2005JA011034. 2

794 Weber, E. J., R. T. Tsunoda, J. Buchau, R. E. Sheehan, D. J. Strickland, W. Whiting, and J. G. Moore, 1985.
795 Coordinated measurements of auroral zone plasma enhancements. *Journal of Geophysical Research:*
796 *Space Physics*, **90**(A7), 6497–6513. 1

797 Weimer, D. R., 1995. Models of high-latitude electric potentials derived with a least error fit of spherical
798 harmonic coefficients. *Journal of geophysical research.*, **100**(A10), 19,595–19,607. 5

799 Wilson, G. R., D. R. Weimer, J. O. Wise, F. A. Marcos, G. R. Wilson, D. R. Weimer, J. O. Wise, and F. A.
800 Marcos, 2006. Response of the thermosphere to Joule heating and particle precipitation. *Journal of*
801 *geophysical research.*, **111**(A10). 1

802 Xiong, C., C. Stolle, P. Alken, and J. Rauberg, 2020. Relationship between large-scale ionospheric field-
803 aligned currents and electron/ion precipitations: DMSP observations. *Earth, planets, and space*, **72**(1),
804 1–22. 5

805 Yeh, K. C., and C.-H. Liu, 1982. Radio wave scintillations in the ionosphere. *Proceedings of the IEEE*, **70**(4),
806 324–360. 2, 2, 2, 4.2.1